Research Square

Preprints are preliminary reports that have not undergone peer review.
They should not be considered conclusive, used to inform clinical practice,
or referenced by the media as validated information.

Dynamic Monitoring of Soil Salinity in Salinized Farmland Using LIBS and UAV-Based Hyperspectral Imaging

Guanghui Dong
Northwest Normal University
Kadambot H. M. Siddique
The University of Western Australia
Weiwei Han
Northwest Normal University
Guoding Zhang
Northwest Normal University
Duixiong Sun
Northwest Normal University
Andong Wang
Northwest Normal University
Maijuan Li
Northwest Normal University
Shaoping Du
Cansu Academy of Agricultural Science
Juan Chen
Cansu Academy of Agricultural Science
Chaonan Tang
Cansu Academy of Agricultural Science
Maogen Su
nwnu_sumg@163.com

Northwest Normal University

Research Article

Keywords: soil salinity, laser-induced breakdown spectroscopy (LIBS), unmanned aerial vehicle hyperspectral imaging (UAV-HSI), data fusion, regional inversion, time-series mapping

Posted Date: November 16th, 2026

DOI: https://doi.org/10.21203/rs.3.rs-10761908/v1

License: This work is licensed under a Creative Commons Attribution 4.0 International License.
Read Full License

Additional Declarations: No competing interests reported.

Dynamic Monitoring of Soil Salinity in Salinized Farmland Using LIBS and UAV-Based Hyperspectral Imaging

Guanghui Dong [1], Kadambot H. M. Siddique [2], Weiwei Han [1], Guoding Zhang [1], Duixiong Sun [1], Andong Wang [1], Shaoping Du [4], Juan Chen [4], Chaonan Tang [4], and Maogen Su [1,2]*

[1]. Key Laboratory of Atomic and Molecular Physics & Functional Materials of Gansu Province, College of Physics and Electronic Engineering, Northwest Normal University, Lanzhou 730070, Gansu, China.

[2]. The UWA Institute of Agriculture, The University of Western Australia, Perth, WA 6001, Australia

[3]. Gansu International Scientific and Technological Cooperation Base of Laser Plasma Spectroscopy, Lanzhou 730070, Gansu, China.

[4]. Vegetable Research Institute, Cansu Academy of Agricultural Science, Lanzhou 730070, Gansu, China.

*Correspondence: Author to whom correspondence should be addressed.

Abstract

To address the challenges of high spatiotemporal heterogeneity and limited model generalization in hyperspectral soil salinity inversion under complex field environments, this study proposes a monitoring framework integrating Laser-Induced Breakdown Spectroscopy (LIBS) and Unmanned Aerial Vehicle-based Hyperspectral Imaging (UAV-HSI). Taking the saline farmlands of Jingtai, Gansu Province, as the study area, six multi-temporal sampling campaigns were conducted. A point-scale fusion model was first established for high-precision salinity estimation. These point-scale estimates served as "surrogate labels" for regional inversion using concurrent UAV-HSI imagery. Continuous salinity maps were subsequently generated through vegetation masking and spatial interpolation. Results indicated a strong complementarity between LIBS and HSI. The fusion model achieved superior point-scale prediction accuracy ($R^2 = 0.989 \pm 0.003$, RMSE = 3.039 ± 0.457 g/kg) compared to single-source models. Wilcoxon tests no statistically significant differences were detected ($p > 0.05$) between regional inversion results derived from surrogate labels versus those from gravimetric ground-truth labels. During the observation period, surface soil salinity exhibited a distinct seasonal trend: higher in spring/summer and lower in autumn/winter. This methodology preserves the efficiency of both proximal and remote sensing while balancing point-scale precision with regional coverage, providing a novel technical pathway for the dynamic monitoring of salinized farmlands.

Keywords: soil salinity; laser-induced breakdown spectroscopy (LIBS); unmanned aerial vehicle hyperspectral imaging (UAV-HSI); data fusion; regional inversion; time-series mapping

1. Introduction

Soil salinization is a primary driver of land degradation across millions of hectares globally, severely constraining cropland quality, sustainable agricultural production, and ecosystem stability(Das et al., 2023).As the demand for dynamic monitoring and precision management of saline farmlands intensifies, soil salinity assessment is transitioning from discrete, lab-based point measurements.(Corwin and Lesch, 2005)toward intelligent, multi-dimensional sensing paradigms that integrate remote sensing with proximal sensing(Corwin and Scudiero, 2019; Hassani et al., 2021; Shoshany et al., 2013; Wang et al., 2025). In this context, developing methodologies that simultaneously offer high detection accuracy and broad regional coverage remains a critical scientific and technical challenge.

UAV-based hyperspectral imaging (UAV-HSI) is widely recognized as an essential tool for farmland-scale salinity monitoring due to its capacity for rapid, non-destructive, and spatially continuous spectral acquisition(Das et al., 2023; Lu et al., 2020).. However,quantifying soil salinity from HSI data in complex field settings remains challenging (Zhan et al., 2025). This is primarily attributed to soil heterogeneity,where spectral responses are confounded by soil moisture, surface roughness, vegetation residue, and varying illumination conditions(Metternicht and Zinck, 2003).Such environmental variations across different periods weaken the generalization capacity of models built on multi-temporal data(Borsoi et al., 2020; Hao et al., 2016; Kahaer and Tashpolat, 2019),tConsequently, the robust cross-temporal and cross-spatial performance of UAV-HSI requires significant enhancement.

To improve monitoring precision, multi-source data fusion has emerged as a focal point, including the synergy between HSI and other remote sensing datasets(He et al., 2025, 2023; Lin et al., 2026)or the integration of remote observations with proximal sensing to enhance regional assessment (Ivushkin et al., 2019; Song et al., 2024).. Despite these advances, existing methods still suffer from low label acquisition efficiency, insufficient model robustness, and limited generalization in complex field conditions.

Laser-induced breakdown spectroscopy (LIBS), as an in situ analytical technique, has been widely applied to the quantitative determination of soil elements(Goueguel et al., 2019; Lin et al., 2024; Ren et al., 2022; Villas-Boas et al., 2020), and has demonstrated higher detection efficiency than conventional point-based detection methods in soil salinity detection(ZHAO et al., 2020).. Meanwhile, studies integrating LIBS with hyperspectral imaging have shown great potential in multiple fields, including quantitative elemental analysis(Li et al., 2025), ore surface visualization (Sandoval-Muñoz et al., 2022), and agricultural product classification(Y. Liu et al., 2022; Zhao et al., 2021). In the rapid, high-resolution visualization of surface elements in materials, the combination of LIBS point measurements and HSI-based spatial inversion has compensated for the limitation of LIBS in areal detection(Zhao et al., 2023). In the detection of Na content in sorghum roots, the integration of LIBS and HSI improved the accuracy of point-based measurements through data fusion(Li et al., 2025).These studies indicate that the advantages of LIBS in proximal elemental sensing

and those of HSI in regional coverage are strongly complementary. However, systematic research is still lacking on how to effectively integrate the two techniques under complex field conditions to develop a soil salinity monitoring method that simultaneously accounts for detection accuracy, label acquisition efficiency, and regional scalability.

Accordingly, this study proposes a soil salinity monitoring framework that fuses LIBS and UAV-HSI. The objectives are: (1) to construct a multi-modal fusion model for robust point-scale salinity estimation; (2) to implement regional-scale spatial extrapolation by using point-scale estimates as surrogate labels for concurrent HSI inversion; and (3) to generate continuous salinity maps using vegetation masking and spatial completion to analyze seasonal dynamics. This framework offers a novel technical route for high-precision, regionalized, and dynamic monitoring of salinized farmlands

2. **Materials and Methods**

2.1 Study Area

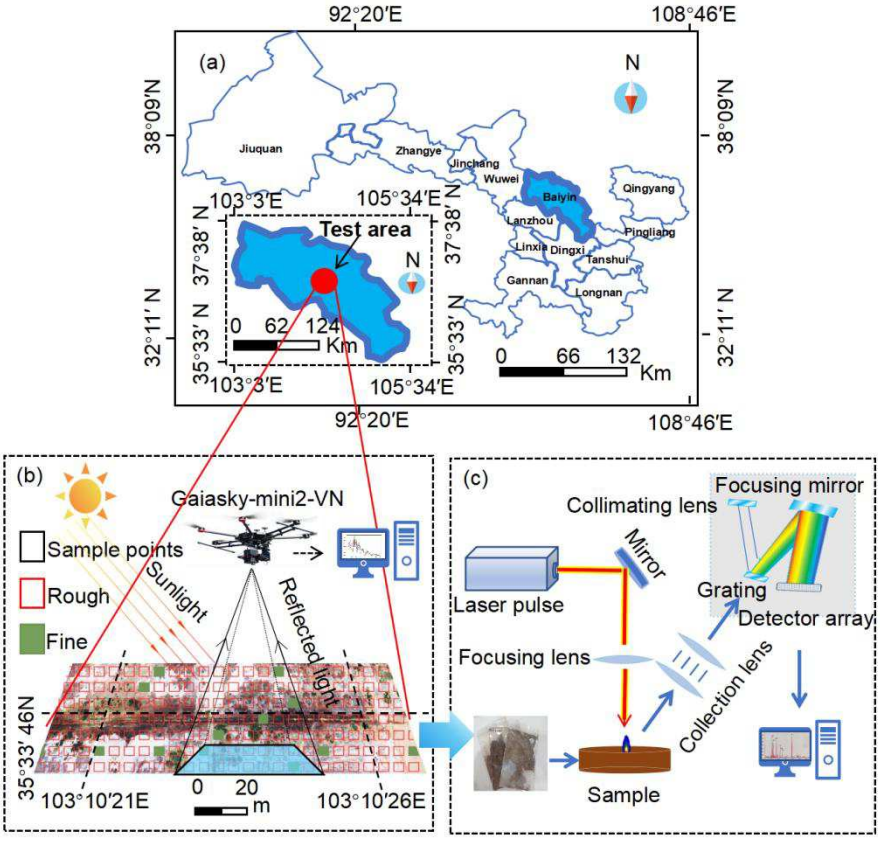


Fig. 1. Study area distribution and data acquisition workflow.(a) Geographic location of the study area.(b) Layout of fixed monitoring points and coverage of hyperspectral imagery.(c) Schematic diagram of the LIBS data acquisition workflow.

Figure 1(a) shows the study area, Lanjian Farm in Jingtai, Gansu Province, located in the transitional zone between the Loess Plateau and the Tengger Desert. The region has an arid climate, and long-term large-scale flood irrigation has led to secondary

salinization. The soils are primarily gray-brown desert soils and calcareous soils, exhibiting a pronounced salinity gradient, making this area an ideal test site for investigating the spatial distribution of soil water-soluble salts and rapid detection methods(Jiao et al., 2018). Figure 1(b) presents the results of the first comprehensive soil electrical conductivity (EC) survey, the distribution of fixed monitoring points, and the coverage of hyperspectral imagery. In this figure, red frames or markers indicate the survey units of the initial EC assessment, green dots represent fixed monitoring points selected based on the survey results, and the light blue area delineates the coverage of individual hyperspectral images. Figure 1(c) illustrates the schematic principle of laser-induced breakdown spectroscopy (LIBS) measurements.

2.2 Sample Collection and Processing

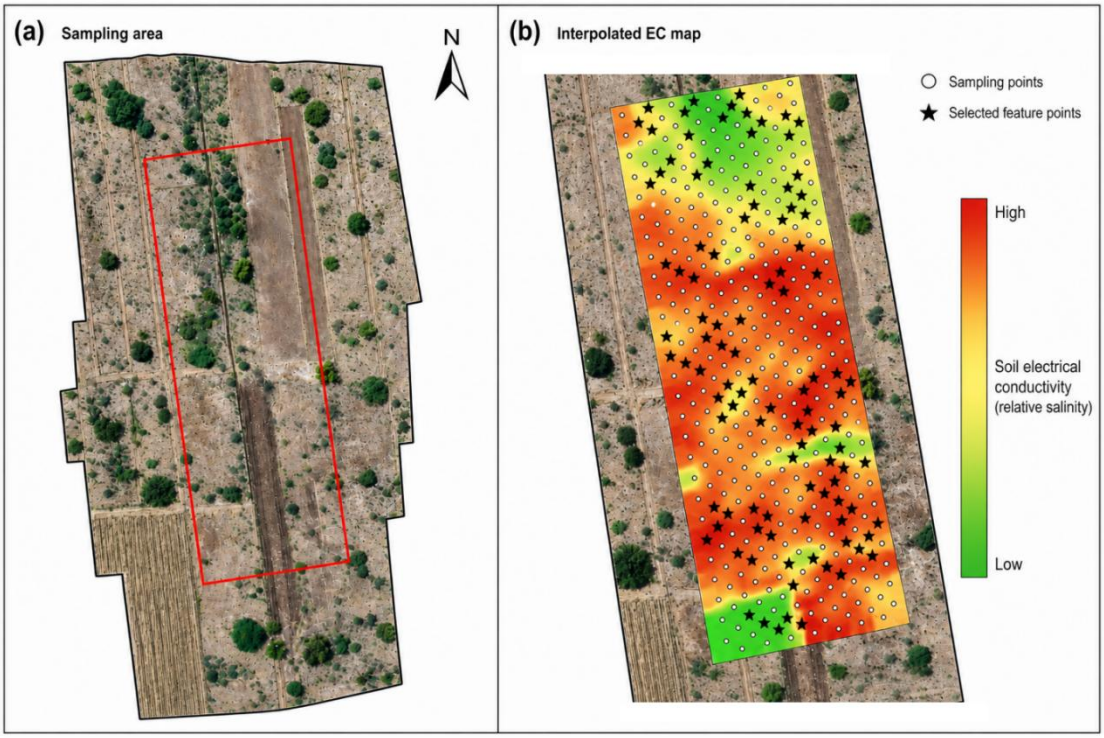


Fig. 2. Schematic diagram of the soil electrical conductivity survey results and the layout of fixed monitoring sites.

Figure 2(b) presents the spatial distribution heatmap of soil electrical conductivity (EC) for the area shown in Figure 1(b). A sampling grid with a 3 m spacing was established, yielding a total of 405 sampling points, at which soil EC was measured to characterize the spatial distribution pattern of soil conductivity in the study area. Based on these measurements, 100 representative fixed monitoring points were selected, and six repeated samplings were conducted across different seasons within one year to analyze the temporal variation of soil salinity. Concurrently, a hyperspectral imaging (HSI) system was used to capture images of the entire sampling area, providing surface reflectance spectral information.

After sampling, plant residues and stones were removed, and the samples were oven-dried at 60 ℃. The dried samples were then ground and sieved through a 200-mesh sieve. Six grams of soil were compressed under 20 MPa pressure into a pellet

approximately 32 mm in diameter, followed by LIBS spectral measurements using a handheld device. Simultaneously, and the soil water-soluble total salt content was determined using the gravimetric method, serving as the reference salinity value for the corresponding plot and as the standard reference for constructing and evaluating the LIBS-HSI fusion model.

2.3 Instruments and Measurement Methods

HSI data were acquired using a GaiaSky-mini2-VN UAV-mounted hyperspectral imager with a spectral range of 400–1000 nm. Data collection was conducted under clear and cloudless weather conditions with wind speeds below 2 m/s. During operation, the UAV flew at an altitude of approximately 150 m and a speed of 7 m/s, and surface hyperspectral images were obtained using the hover-and-push-broom scanning mode. The image coverage was approximately 81 m × 35 m. In addition, a 2 × 2 m gray calibration tarp with 50% reflectance, calibrated by the National Institute of Metrology, was placed on the ground for radiometric correction(Sun et al., 2021; Tang et al., 2023). Before image acquisition, white reference data and dark background data were collected for system noise removal. Geometric correction was then performed to reduce the geometric distortion introduced by platform attitude variation and terrain undulation, thereby improving the spatial positioning accuracy of ground objects(Yu et al., 2024).Based on the latitude and longitude information of the sampling points described in Section 2.2, the corresponding locations were identified in the imagery, and 250 pixels around each sampling point were selected to form a region of interest (ROI). The surface reflectance of each pixel within the ROI was extracted to obtain the HSI spectral features of the corresponding sampling point.

2.4 Data Processing

Outlier spectra were identified using the interquartile range (IQR) criterion. Spectral observations falling outside $Q_1-1.5IQR$ and $Q_3+1.5IQR$ were considered abnormal and removed before subsequent averaging. Subsequently, every 10 LIBS spectra and every 10 HSI spectra were averaged to reduce the influence of random noise on the results. Prior to feature selection, the HSI spectra were first transformed using first-order derivatives to enhance local spectral variation and reduce the effects of background noise and baseline drift(Bañón et al., 2021), thereby effectively highlighting spectral differences caused by variations in total water-soluble soil salts. Pearson correlation coefficients were then used to identify spectral features sensitive to soil salinity variation by analyzing the linear relationships between LIBS spectra, original HSI spectra, first-derivative HSI spectra, and total water-soluble soil salt content(Schober et al., 2018).Specifically, for the LIBS spectral intensity at each wavelength within the 200–1000 nm range, as well as the HSI surface reflectance and its first-derivative values within the 400–1000 nm range, Pearson correlation coefficients with total water-soluble soil salt content were calculated to quantify the linear representational ability of different spectral variables with respect to the target variable. The formula for calculating the Pearson correlation coefficient is as follows:

$$r_i = \frac{\sum_k^n (I_{ik} - I_i)(y_k - y)}{\sqrt{\sum_{k-1}^n (I_{ik} - \overline{I_i})^2} \sqrt{\sum_{k-1}^n (y_k - \bar{y})^2}}$$

where the spectral intensity of the kth sample at the ith wavelength is denoted I_{ik},the corresponding target variable is represented by y_k,$\overline{I_i}$ and $\bar{y}$ and are the mean values of the spectral intensity and the target variable, respectively. In this way, a correlation metric was obtained for each wavelength. Subsequently, sensitive hyperspectral bands significantly correlated with total water-soluble soil salt content were selected to construct spectral indices, and the specific formulations are presented in Table I. The linear relationships among these spectral indices, LIBS characteristic spectra, and total water-soluble soil salt content were then analyzed. Finally, the LIBS feature data, hyperspectral feature data, and spectral indices were used as input variables for the model.

Table I. In the table,R_B,R_G, R_R and R_{NIR} represent the characteristic surface reflectance in the blue, green, red, and near-infrared bands, respectively. The construction methods of the spectral salinity indices and their corresponding references are listed under each category.

Index category	Index name	Expression
盐碱化光谱指数 (Douaoui et al., 2006; Khan et al., 2005)	Salinity Index（SI）	$SI = \sqrt{R_B \times R_R}$
	Salinity Index 1（SI1）	$SI1 = \sqrt{R_G \times R_R}$
	Salinity Index 2（SI2）	$SI2 = \frac{R_R}{R_{NIR}}$
	Salinity Index 3（SI3）	$SI2 = \frac{R_B}{R_R}$
归一化差值类指数 (Chen et al., 2025)	Normalized Difference Salinity Index1（NDSIRN）	$NDSI_{RN} = \frac{R_R - R_{NIR}}{R_R + R_{NIR}}$
	Normalized Difference Salinity Index2（NDSIBN）	$NDSI_{BN} = \frac{R_B - R_{NIR}}{R_B + R_{NIR}}$
	Normalized Difference Salinity Index3（NDSIGN）	$NDSI_{GN} = \frac{R_G - R_{NIR}}{R_G + R_{NIR}}$
复合与增强型盐碱指数(Fernández-Buces et al., 2006)	Combined Soil Salinity Index（CSSI）	$CSSI = \frac{R_B + R_G}{R_R + R_{NIR}}$
	Combined Spectral Response Index（COSRI）	$COSRI = (\frac{R_B + R_G}{R_R + R_{NIR}}) \times \frac{R_{NIR} - R_R}{R_{NIR} + R_R}$

2.5 Model Development

Figure 3 illustrates the framework for LIBS–HSI data fusion and visualization, which comprises three stages: point-level salinity prediction, regional salinity inversion, and salinity mapping. First, based on the correlation analysis results described in Section 2.4, variables highly correlated with soil water-soluble total salt content were selected from the LIBS and HSI datasets to construct the LIBS point-feature spectral dataset (D_1), the HSI spectral feature dataset (D_2), and the spectral index dataset (D_3). Here, D_1 represents LIBS features at sub-point locations, while D_2 and D_3 are derived from hyperspectral imagery, reflecting the spectral characteristics and spectral index information of each pixel, respectively. To improve consistency between image and sampling scales, the raw HSI data were first aggregated using a 5 × 5 neighborhood mean. Subsequently, D_2 and D_3 features corresponding to the LIBS sampling points were extracted via georeferencing and fused with D_1 to construct a multimodal point-level dataset.

Point-level salinity prediction was performed using a multimodal fusion regression network. The model takes the multimodal point-level dataset as input and first applies a feature attention mechanism to adaptively weight the input variables, enhancing key information while suppressing redundant noise. The weighted features are then fed into a two-layer fully connected regression network to predict soil water-soluble total salt content at each sampling point. To improve model stability and generalization, Batch Normalization and Dropout layers were incorporated into the network. The model was trained using the Adam optimizer with a learning rate of 0.001, and the loss function was defined as mean squared error (MSE).

Considering the variations in imaging conditions and spectral distributions across different hyperspectral acquisition periods, regional salinity inversion was performed using a period-specific modeling strategy. For each acquisition period, D2 and D3 features were extracted from the corresponding imagery, and the point-level features at sampling locations were obtained. Point-level salinity predictions from the previous-stage fusion model were converted to plot-scale reference labels to train the hyperspectral inversion model for that period. After training, the model was applied to the entire image acquired during the same period to achieve regional-scale salinity inversion. The regional inversion model also employed a regression network with a feature attention mechanism, consisting of a backbone of three fully connected layers with 256, 128, and 64 neurons in the hidden layers, respectively. The model was trained using the Adam optimizer with a learning rate of 0.0005, the mean squared error (MSE) as the loss function, and EarlyStopping was incorporated to prevent overfitting.

To mitigate the influence of vegetation cover on regional salinity inversion, the soil-adjusted vegetation index (SAVI) was applied to mask the hyperspectral imagery, retaining only areas dominated by bare soil or salt crust for prediction. The SAVI is calculated using the following formula:

$$SAVI = \frac{(NIR - Red)}{(NIR + Red + L)}(1 + L)$$

In the equation, NIR represents the near-infrared reflectance at 800 nm, Red represents the red reflectance at 651 nm, and L is the soil adjustment factor, which was

set to 1 in this study. Areas with SAVI values less than 0 were considered valid soil pixels. After masking, only the valid pixels were standardized and subjected to model prediction to obtain the initial spatial distribution of soil water-soluble total salts.

To enhance the continuity of the salinity distribution map, the few missing pixels resulting from the masking process were spatially imputed using the nearest-neighbor mean method. For each missing pixel, the Euclidean distances to all valid pixels were calculated, and the imputed value was set as the mean of the predictions of the nearest valid pixels, as follows:

$$Z(x_i) = \frac{1}{k} \sum_{x_j \in N_k(x_i)} z(x_j), x_i \in \Omega_{\mathrm{NaN}}$$

Let Ω_{NaN} denote the set of missing pixels, $N_k(x_i)$ the set of valid pixels nearest to a missing pixel m∈M and $Z(x_i)$the predicted values of the valid pixels. Finally, the imputed inversion results were visualized using a unified color scale to generate the spatial distribution map of soil water-soluble total salts in the study area.

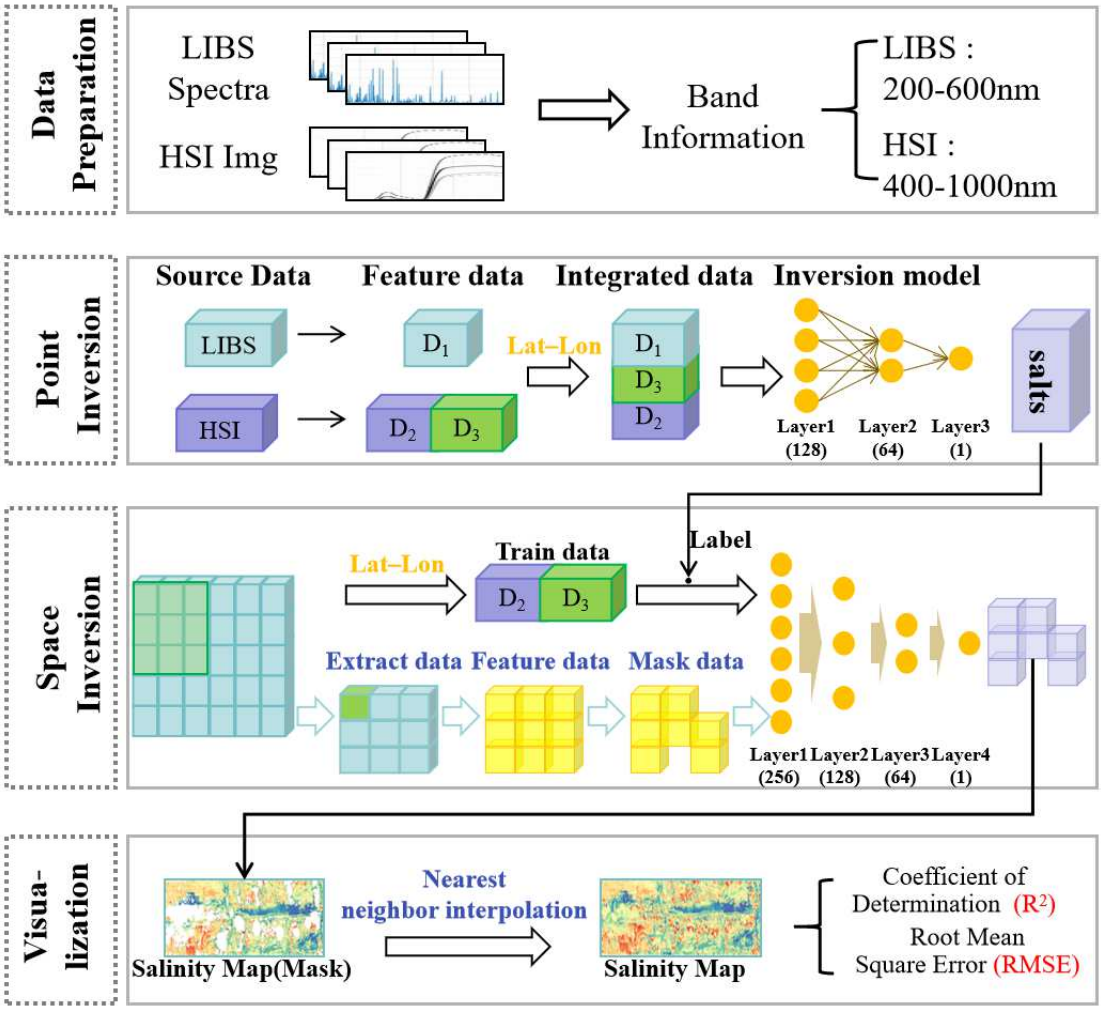


Fig 3 Algorithm Flowchart

2.6 Model Evaluation

Model evaluation followed the principle of maintaining consistency between the

hierarchical level of the supervised labels and that of the cross-validation grouping. Each fixed monitoring area at a given monitoring period was associated with only one area-level gravimetrically measured reference value of water-soluble total salt (WSTS), whereas multiple LIBS and HSI spectral observations within that area shared the same reference label. These spectral observations therefore cannot be regarded as statistically independent samples. Accordingly, a grouped cross-validation strategy based on the combination of "fixed monitoring area × monitoring period" was adopted. All observations collected from the same fixed monitoring area during the same period were assigned to a single group, and each group was restricted to either the training set or the validation set. This strategy prevents correlated observations sharing the same supervised label from being randomly split across training and validation sets, thereby reducing pseudo-independence and potential information leakage, minimizing the risk of overestimating model performance, and providing a more reliable assessment of model generalization.

Model performance was evaluated using the root mean squared error (RMSE) and the coefficient of determination (R^2)(Chicco et al., 2021), calculated as follows:

$$R^2(y,\hat{y}) = 1 - \frac{\sum_{i=1}^{n}(y-\hat{y}_i)^2}{\sum_{i=1}^{n}(y-\bar{y}_i)^2}$$

$$RMSE = \sqrt{\frac{\sum_{i=1}^{n}(y-\hat{y}_i)^2}{n}}$$

Here, n denotes the number of samples. The coefficient of determination (R^2) indicates the correlation between predicted and observed values, with values closer to 1 representing better model performance. The root mean squared error (RMSE) quantifies the deviation between predicted and observed values, with smaller RMSE values indicating higher prediction accuracy.

For the point-scale soil salinity sensing model, all samples collected over the six monitoring periods were pooled and incorporated into a unified modeling and evaluation framework to assess model performance for unseen samples under mixed spatiotemporal conditions. The grouped cross-validation strategy described above was applied, with each combination of fixed monitoring area and monitoring period treated as an independent grouping unit. All observations associated with the same area–period combination were kept together and assigned exclusively to either the training or validation set, thereby preventing observations sharing the same WSTS reference value from being split across the two subsets. Within each cross-validation fold, feature selection, estimation of standardization parameters, and model training were performed exclusively using the training data, and the resulting feature-selection criteria and preprocessing parameters were subsequently applied to the corresponding validation set. Thus, the validation data remained independent of the model-development procedure, reducing the risk of pseudo-independence and information leakage. Model performance was quantified using the coefficient of determination (R^2) and root mean square error (RMSE), and the mean and standard deviation of these metrics across all folds were used to characterize the predictive accuracy and stability of the model for

unseen area–period combinations.

To further assess the model's robustness to environmental variation and distributional shifts among different monitoring periods, an independent cross-period validation was subsequently conducted. The complete dataset was divided into six mutually exclusive subsets according to monitoring period, and a six-fold leave-one-period-out validation strategy was employed. In each fold, all samples from one monitoring period were held out as an independent test set, while samples from the remaining five periods were used for model training. Thus, data from the held-out period were completely excluded from model development. By sequentially using each of the six monitoring periods as the independent test set, this procedure simulated a practical scenario in which a model developed using previously observed periods is applied to a new, unseen monitoring period, while also allowing temporal variations in predictive performance to be quantified. As in the mixed spatiotemporal validation, feature selection, parameter estimation for standardization, and model training were conducted solely using the training-period data. R^2 and RMSE were then calculated separately for each held-out period, and their means and standard deviations were used to characterize the cross-period predictive capability and stability of the model.

In addition, to benchmark the proposed point-scale salinity sensing model against conventional data-driven approaches, partial least squares regression (PLSR), random forest (RF), and support vector machine (SVM) models were selected as reference methods under identical sample partitioning, input data, preprocessing procedures, and evaluation criteria. PLSR was used to represent a typical linear multivariate regression approach, RF to represent a nonlinear ensemble-learning method, and SVM to characterize kernel-based nonlinear modeling capability. By comparing the R^2 and RMSE values obtained by the different models under both mixed spatiotemporal cross-validation and independent cross-period validation, the proposed model was systematically evaluated in terms of quantitative prediction accuracy, model stability, and cross-period generalization performance.

For the regional-scale salinity inversion model, the objective was to spatially extend point-level predictions to the regional scale within hyperspectral imagery acquired during the same sampling period. Thus, a single-period training–validation strategy was adopted to evaluate the model's spatial generalization capability. Specifically, for each sampling period, HSI spectral features and spectral indices extracted at fixed monitoring point locations were used as inputs, and high-accuracy point-level salinity predictions from the previous stage served as proxy labels. To prevent information leakage caused by using first-stage model outputs directly for the same samples in the second stage, all proxy labels used for regional inversion were derived from out-of-fold predictions within the first-stage grouped cross-validation framework. In other words, for any "fixed monitoring plot × sampling period" sample, its proxy label was generated solely by the first-stage fusion models that had not been trained on that sample, ensuring statistical independence relative to the second-stage regional inversion training data. The regional inversion sample set for the period was then constructed and split into training and validation sets for model training and evaluation. It should be emphasized that this stage assesses the model's ability to

generalize spatially under temporally consistent conditions.

3. Results and Discussion

3.1 Spectral Analysis and Feature Selection

Based on the feature selection procedure described in Section 2.4, the correlations between LIBS elemental features, HSI sensitive wavelengths, spectral indices, and soil water-soluble total salt content were further analyzed to identify key variables that are most responsive to salinity changes and complementary across data sources. The results indicate notable differences among the data sources in characterizing soil salinity: LIBS features primarily capture salinity-related elements and mineral background information; HSI sensitive wavelengths better reflect local spectral variations induced by surface salt enrichment; and spectral indices further enhance the response of surface reflectance characteristics to salinity variations.

Based on preliminary experience and the NIST spectral database, the elements and corresponding spectral lines closely associated with soil water-soluble total salts were identified. As shown in Figure 4(a), the acquired LIBS spectra contained characteristic lines of elements such as Fe, Si, Al, Ca, and Na. For the hyperspectral imagery data, the reflectance spectra within the 400–1000 nm range were first subjected to first-order derivative processing to emphasize local spectral variations caused by changes in soil composition. Subsequently, correlation analysis and sensitive wavelength selection were performed within the blue, green, red, and near-infrared spectral regions(Bannari et al., 2018; Zhang et al., 2016). After identifying sensitive wavelengths, the corresponding original reflectance values were extracted to construct the HSI spectral feature dataset (D_2), from which spectral indices were calculated to form D_3 for subsequent multimodal fusion modeling.

As shown in Figure 4(c), the features associated with Fe and Si exhibit an overall negative correlation, consistent with previous studies reporting that extractable Si and Fe decrease with increasing salinity under salt treatment conditions(Saleh et al., 2013). This suggests that these elements primarily reflect the combined response of soil mineral composition and their bioavailable forms under the background of salt accumulation. In contrast, features associated with Al and Ca display weak to moderate positive correlations, while the Na I characteristic line shows the strongest positive correlation with soil water-soluble total salt content, with a correlation coefficient of 0.54. This indicates that Na-related elements are the most sensitive to salinity variations in the study area, consistent with previous investigations of ion composition in saline soils of the Yellow River irrigation region in Gansu(Si-Cun et al., 2014). Overall, the LIBS spectral features reflect not simple changes in individual element concentrations but rather the integrated response resulting from salt accumulation, variations in elemental bioavailability, and the soil mineral background.

As shown in Figure 4(c), the first-order derivative of the HSI spectra exhibits a significant overall negative correlation with soil water-soluble total salt content, with correlation coefficients all below −0.65. Among these, the first-order derivative in the

green spectral region shows the strongest correlation, reaching a maximum of −0.84. Further inspection of the first-order derivative curves indicates that the values are generally positive within the visible spectral range and negative within the near-infrared range. This suggests that, as soil water-soluble total salt content increases, the local spectral shapes across different wavelengths undergo systematic changes. In the visible spectral range, surface salt enrichment and the formation of salt crusts increase soil surface reflectance(Howari et al., 2002)and alter surface roughness and scattering characteristics(Metternicht and Zinck, 2003). As a result, the overall HSI spectra of the soil exhibit enhanced reflectance, the amplitude of local ascending slopes diminishes, and the reflectance differences between adjacent bands decrease, leading to reduced local spectral slopes, which manifests as a decrease in first-order derivative values with increasing salinity. At 904.4 nm, the first-order derivative is negative and exhibits a significant negative correlation with soil water-soluble total salt content, indicating that the rate of decrease in reflectance with increasing wavelength is further enhanced as salinity increases. This finding is largely consistent with previous studies reporting pronounced spectral responses of saline soils near 900 nm(Dehaan and Taylor, 2002)

In addition, laboratory studies on chloride salt crusts conducted by Freire et al. demonstrated that soil surface reflectance generally decreases with increasing salt concentration, with a more pronounced decline observed under Ca salt conditions(Pessoa et al., 2015).This phenomenon is consistent with the LIBS results of the present study, which revealed an enhanced response of Ca-related features with increasing soil water-soluble total salt content, suggesting that the spectral variation at 904.4 nm may not only be associated with surface salt enrichment but may also be influenced by the accumulation of Ca-related salts and their effects on surface scattering characteristics. Furthermore, previous studies have indicated that the 800 – 1000 nm range can be regarded as a sensitive region for iron oxide-related absorption features. Therefore, the spectral response at 904.4 nm may also be partially affected by the background influence of Fe oxides. This finding is consistent with the significant correlation observed between the Fe I feature in LIBS spectra and soil water-soluble total salt content, indicating that both HSI and LIBS data reveal the potential role of Fe-related information in soil salinity characterization.

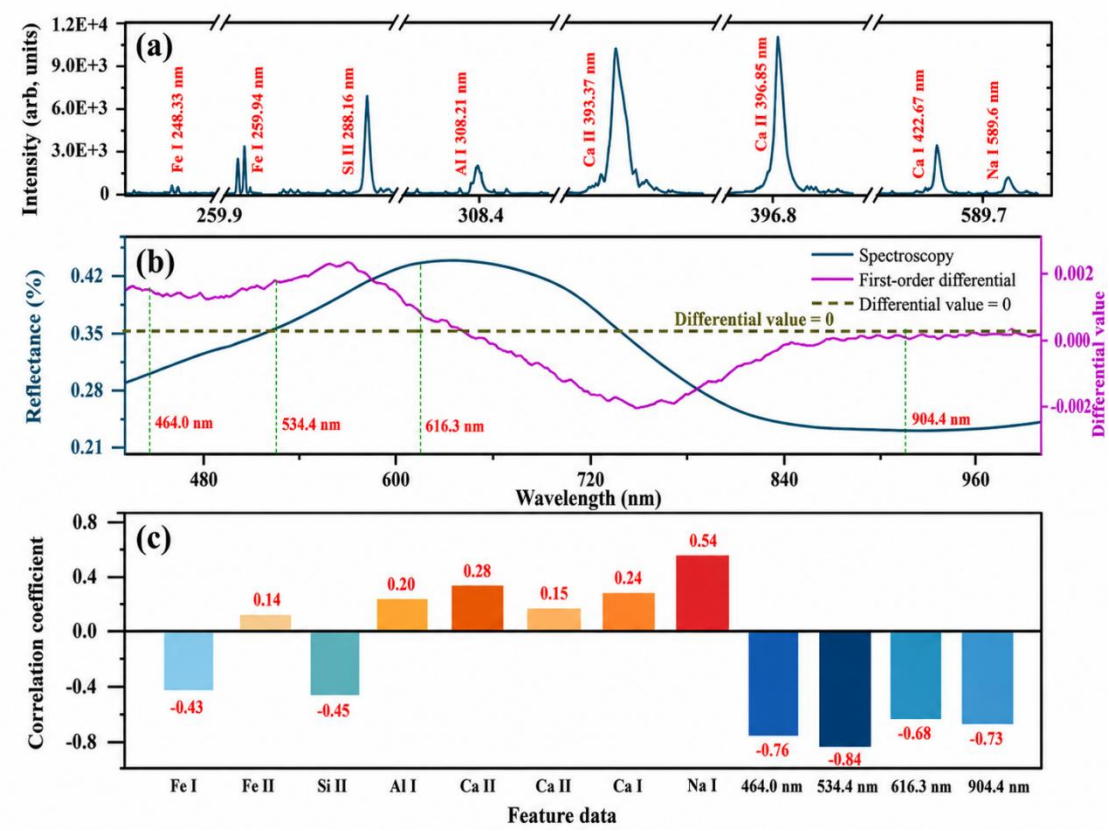


Fig 4. Sensitive feature selection results for LIBS and HSI.(a) Characteristic spectral lines of typical elements in LIBS;(b) Original HSI reflectance spectra and their first-order derivative curves;(c) Correlation coefficients between LIBS elemental features and HSI sensitive wavelengths with soil water-soluble total salt content

Figure 5 illustrates the correlations between nine spectral indices (SI, SI1, SI2, SI3, NDSIRN, NDSIBN, NDSIGN, CSSI, and COSRI), LIBS elemental features (Fe I, Fe II, Si I, Al I, Ca II, Ca II, Ca I, and Na I), and soil water-soluble total salt content. Overall, the spectral indices exhibit distinct relationships with LIBS elemental features and water-soluble salts, indicating that the spectral indices do not simply replicate the original sensitive wavelength information but rather enhance and reorganize the salinity-related spectral responses through combinations of different bands. Meanwhile, the LIBS elemental features display moderate to strong correlations among themselves, suggesting that elements such as Fe, Si, Al, Ca, and Na respond in a partially coordinated manner. However, the directions and strengths of the correlations between the spectral indices and these elements are not consistent, indicating that the spectral indices primarily capture surface reflectance characteristics and surface salt accumulation processes rather than information about individual element concentrations.

Further analysis revealed that most spectral indices exhibit strong negative correlations with Fe- and Si-related features, whereas their correlations with Ca- and Na-related features are comparatively weaker, though still predominantly negative. This suggests that the spectral indices do not primarily enhance the direct elemental responses of the main salinity-controlling elements, but rather capture integrated

spectral information associated with soil mineral background, surface reflectance variations, and local spectral shape reconstruction. In combination with the LIBS feature analysis presented earlier, Fe and Si features are more indicative of the soil background, while HSI spectral indices are more sensitive to surface salt enrichment, including salt crust formation, brightness changes, and alterations in scattering conditions. Therefore, although spectral indices are correlated with soil water-soluble total salt content, their mechanism primarily reflects salinity variations indirectly through surface spectral responses, rather than directly representing the concentrations of salinity-related elements such as Na and Ca.

In summary, LIBS characteristic spectral lines, the original reflectance at HSI sensitive wavelengths selected via first-order derivative analysis, and the spectral indices constructed from these wavelengths each capture variations in soil water-soluble total salts from three complementary perspectives: elemental responses, local spectral shape changes, and enhancement through band combination. Specifically, LIBS features primarily highlight salinity-related elements and mineral background information; the original reflectance corresponding to HSI sensitive wavelengths more effectively reflects local spectral shape variations induced by surface salt enrichment; and spectral indices further amplify the response of surface reflectance features to salinity changes.

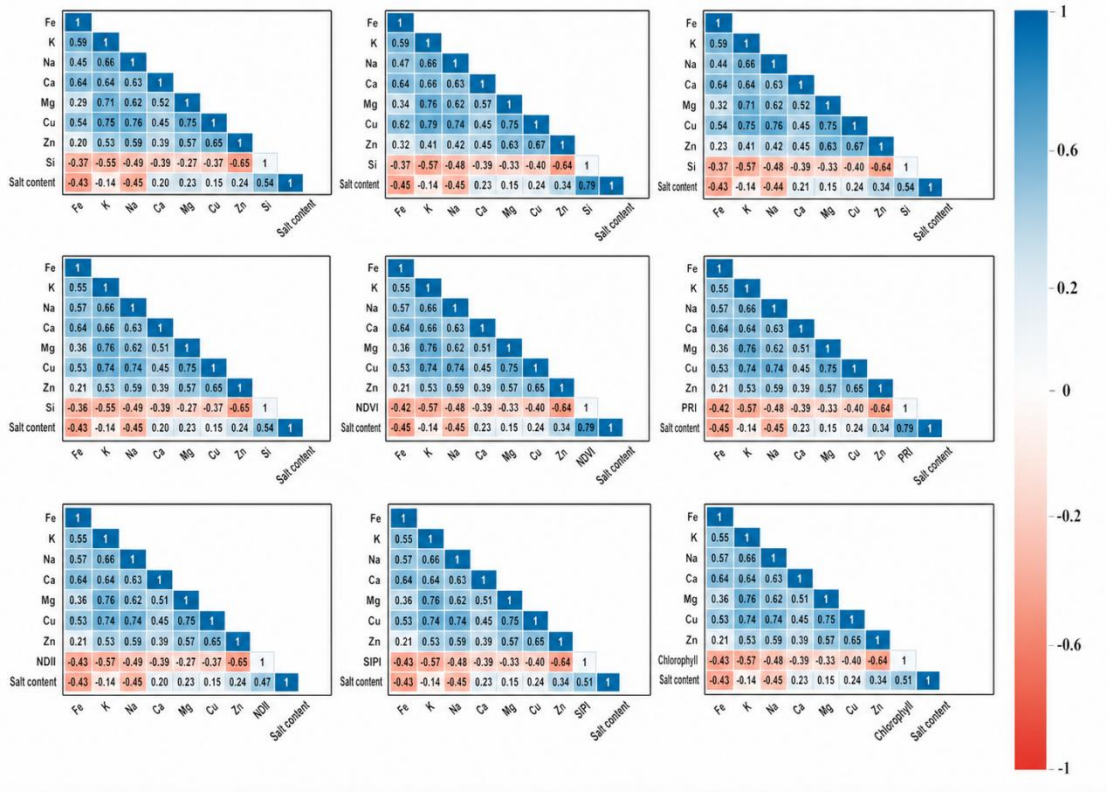


Figure 5. Heatmap of the correlations between spectral indices, LIBS elemental features, and soil water-soluble total salt content. Rows and columns represent LIBS elemental features, spectral indices, and soil water-soluble total salt content, respectively. The color indicates the magnitude and direction of the correlation coefficients.

These results indicate that the salinity information captured by different data sources is highly complementary. Therefore, in this study, Fe I, Si I, Al I, Ca II, Ca I, and Na I were selected as the LIBS feature data. For the HSI spectra, the original reflectance at 484 nm, 534.4 nm, 616.3 nm, and 904.4 nm was selected as feature data. These were then used, along with spectral indices, to construct the D_1, D_2, and D_3 datasets, providing the feature basis for subsequent multimodal fusion modeling.

3.2 Model Performance Comparison and Optimal Model Selection

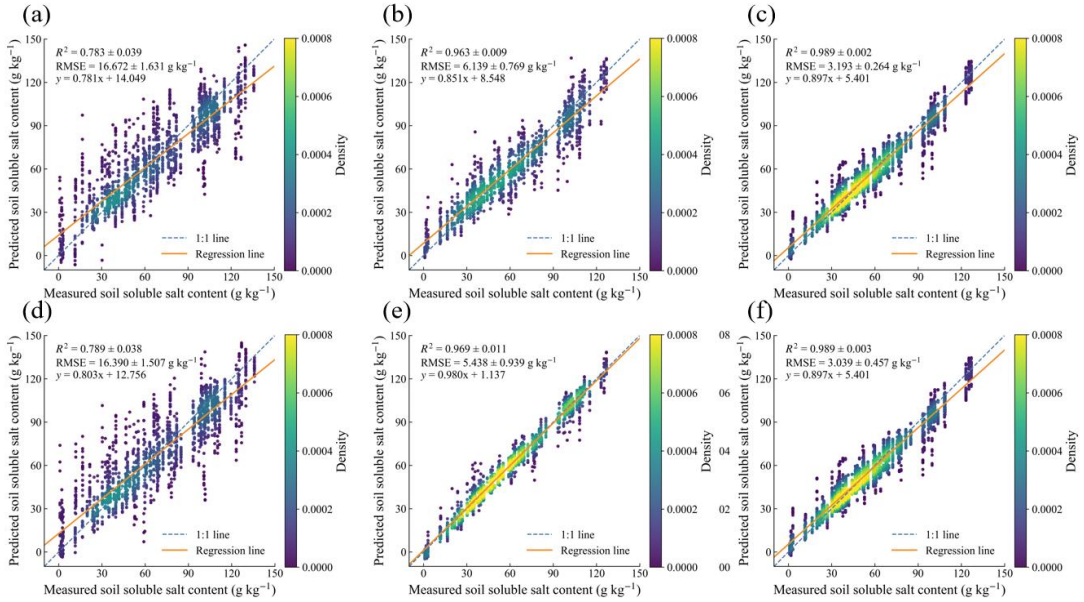


Figure 6. Comparison of point-level soil water-soluble total salt predictions under different input data combinations and network architectures. (a – c) Model results based on HSI data, LIBS data, and fused data, respectively; (d – f) Model results based on HSI data, LIBS data, and fused data with the attention mechanism incorporated. The x-axis represents measured soil water-soluble total salt content, and the y-axis represents predicted values. The blue dashed line indicates the 1:1 line, and the orange solid line indicates the regression fit. Color represents the density of sample points in the two-dimensional space.

To compare the predictive capability of different data sources and network architectures for soil water-soluble total salt content under mixed spatiotemporal conditions, all spectral samples collected across different sampling times and locations were incorporated into a unified validation framework, as shown in Figure 6, to assess each model’s generalization to unseen samples. Panels 6(a) – (c) present the point-level prediction results based on HSI data (D_2 + D_3), LIBS data (D_1), and fused data (D_1 + D_2 + D_3), respectively. Panels 6(d) – (f) show the corresponding results when the attention mechanism is incorporated, based on HSI data (D_2 + D_3), LIBS data (D_1), and fused data (D_1 + D_2 + D_3), respectively. This analysis addresses two key questions: first, which combination of “dataset + model framework” achieves the optimal point-level prediction performance; and second, whether different data sources exhibit varying adaptability to unseen samples under spatiotemporal heterogeneity.

Overall, model performance varied markedly depending on the input data source and network architecture. Point-level prediction models constructed using LIBS data and fused data both exhibited strong linear relationships between predicted and measured soil water-soluble total salt content. In contrast, models based solely on HSI data demonstrated relatively lower accuracy, indicating that different data sources differ significantly in their ability to characterize soil water-soluble total salts, with such differences being particularly pronounced under mixed spatiotemporal conditions.

For the HSI-only model, without the attention mechanism, the model achieved an R^2 of 0.783 ± 0.009 and an RMSE of 16.672 ± 1.631 g/kg; incorporating the attention mechanism slightly increased R^2 to 0.799 ± 0.015, with negligible change in RMSE. Examination of the scatter distribution shows that, although the attention mechanism brings high-density sample regions closer to the 1:1 line, the overall concentration remains limited, especially in the mid-to-high salinity range, where notable dispersion persists. This suggests that, while HSI data can reflect spectral changes caused by surface salt accumulation, its quantitative ability to represent soil water-soluble total salts under complex field conditions involving varying sampling times and spatial locations remains limited, and is susceptible to interference from surface background, roughness, salt crust distribution, and environmental variability. Consequently, the generalization capability of the HSI-only model under spatiotemporal heterogeneity is relatively weak.

By comparison, models based on LIBS data (D1) exhibited significantly higher accuracy than the HSI-only model. Without the attention mechanism, the LIBS model achieved R^2 = 0.963 ± 0.009 and RMSE = 6.159 ± 0.969 g/kg; with the attention mechanism, R^2 further increased to 0.969 ± 0.001 and RMSE decreased to 5.438 ± 0.479 g/kg. From the scatter density distribution, the introduction of the attention mechanism concentrated the high-density sample regions closer to the 1:1 line, reducing overall sample dispersion and further enhancing the consistency between predicted and measured values. These results indicate that elemental composition information captured by LIBS provides a more direct diagnostic capability for soil water-soluble total salts, and that the attention mechanism can further enhance the contribution of key elemental features, improving both model accuracy and stability.

Further comparison of fused model results shows that combining D1, D2, and D3 substantially improved model performance. Without the attention mechanism, the fused model achieved R^2 = 0.989 ± 0.002 and RMSE = 3.161 ± 0.264 g/kg, significantly outperforming the single-source models, highlighting the complementary nature of LIBS elemental information and HSI surface spectral data. Incorporating the attention mechanism, R^2 remained high (0.989 ± 0.003) and RMSE slightly decreased to 3.039 ± 0.457 g/kg, indicating that when multimodal features are already effectively fused, the attention mechanism provides limited additional improvement, but can still optimize prediction errors to some extent.

In summary, the results shown in Figure 6 indicate that the combination of attention mechanism and fused data (D1 + D2 + D3) achieves the optimal point-level prediction performance, outperforming both HSI- and LIBS-only models. Moreover, compared with introducing the attention mechanism alone, data fusion contributes more

substantially to model improvement, demonstrating that multimodal feature integration provides a more comprehensive representation of soil water-soluble total salt variation. These findings highlight that the complementarity of input information is key to enhancing point-level prediction accuracy. Importantly, these results further demonstrate that HSI-only models exhibit relatively limited robustness to unseen area–period combinations under mixed spatiotemporal conditions, whereas multimodal fusion substantially improves both the accuracy and stability of point-scale WSTS prediction.

To further evaluate the model's adaptability to environmental variations and distributional shifts across different monitoring periods, the Point Model was compared with PLSR, RF, and SVM under identical sample partitioning, input data, preprocessing procedures, and evaluation metrics, as shown in Table 2. The Point Model exhibited consistently high predictive performance across all six periods (T1–T6), with R^2 values ranging from 0.9721 to 0.9901 and an average R^2 of 0.9798. Its RMSE ranged from 3.941 to 5.956 g/kg, with a mean value of only 4.773 g/kg. In comparison, the mean R^2 values of PLSR, RF, and SVM were 0.6955, 0.4493, and 0.7785, respectively, while their corresponding mean RMSE values were 17.190, 40.082, and 12.074 g/kg. Notably, the standard deviations of R^2 and RMSE for the Point Model across the six periods were only 0.0078 and 0.931 g/kg, respectively. These results indicate that the Point Model not only achieved higher predictive accuracy but also exhibited less performance variation across monitoring periods, demonstrating stronger cross-period stability and adaptability.

Table Ⅱ Cross-period prediction performance of different models for soil WSTS estimation

Period	Metric	PLSR	RF	SVM	Point Model
T1	R^2	0.6443	0.4243	0.7286	0.9723
	RMSE(g/kg)	24.891	40.334	11.489	4.237
T2	R^2	0.6491	0.3821	0.8235	0.9821
	RMSE(g/kg)	13.418	35.562	9.934	5.956
T3	R^2	0.6554	0.4198	0.7351	0.9751
	RMSE(g/kg)	14.784	29.931	10.864	3.981
T4	R^2	0.7451	0.5862	0.8412	0.9871
	RMSE(g/kg)	17.462	49.232	10.326	4.611
T5	R^2	0.7392	0.4952	0.6988	0.9901
	RMSE(g/kg)	12.681	37.612	13.491	3.941
T6	R^2	0.7397	0.3881	0.8438	0.9721
	RMSE(g/kg)	19.902	47.823	16.341	5.912

3.3 Regional-Scale Salinity Inversion Results

To further evaluate the capability of hyperspectral models for regional inversion under the same temporal conditions and to assess the impact of different label sources on model performance, hyperspectral regional inversion models were constructed based on point data from each period. This section focuses on two primary questions: first, compared with single-source hyperspectral models under mixed spatiotemporal conditions, does labeling with the stage-one salinity sensing results enhance the predictive ability of hyperspectral data for soil water-soluble total salt content within the same period? Second, when the out-of-fold predictions from the stage-one fusion model are used as proxy labels, can the resulting regional inversion performance match that obtained using traditional gravimetric measurements of water-soluble total salt content。

The results indicate that hyperspectral regional inversion models constructed within the same period exhibited overall performance significantly superior to single-source HSI models under mixed spatiotemporal conditions. As shown in Figures 6(a) and 6(d), the point-based prediction model relying solely on HSI data (D_2+D_3) under mixed spatiotemporal conditions achieved R^2 values ranging from 0.783 to 0.799, with an RMSE of approximately 16.672 g/kg. In contrast, under same-period conditions, regional inversion models constructed using gravimetric labels attained R^2 values of 0.787 – 0.962 and RMSE values of 5.059 – 11.368 g/kg across periods, whereas models constructed with proxy labels achieved R^2 values of 0.711 – 0.936 and RMSE values of 6.770 – 14.210 g/kg.

As shown in Table III, the majority of regional models constructed under same-period conditions achieved R^2 values above 0.8 and RMSE below 10 g/kg, consistently outperforming single-source HSI models under mixed spatiotemporal conditions. This indicates that restricting hyperspectral data to the same period effectively mitigates spatiotemporal heterogeneity caused by temporal and spatial variability, thereby enhancing the quantitative characterization of soil water-soluble total salt content. The findings further suggest that obtaining high-accuracy point salinity information via a fusion model, followed by same-period hyperspectral regional inversion, constitutes an effective strategy for achieving stable salt predictions at the regional scale.

A comparison of regional inversion results based on the two label sources revealed moderate period-to-period variations but relatively small differences in overall performance. Across the six monitoring periods, models trained using gravimetric labels achieved a mean R^2 of 0.856 and a mean RMSE of 8.901 g/kg, whereas those trained using proxy labels achieved a mean R^2 of 0.840 and a mean RMSE of 9.065 g/kg. These results indicate that the two labeling strategies produced broadly similar regional inversion performance at the aggregate level.

Paired Wilcoxon signed-rank tests detected no statistically significant differences in either R^2 or RMSE between the gravimetric-label and proxy-label models under the present experimental conditions ($p > 0.05$). Although the relative performance of the two labeling strategies varied among individual monitoring periods, the use of proxy labels did not result in a statistically detectable overall deterioration in regional inversion performance. It should be emphasized, however, that the absence of a

statistically significant difference does not by itself demonstrate statistical equivalence between the two labeling strategies.

Overall, regional hyperspectral inversion models constructed under temporally consistent conditions achieved higher predictive performance than the HSI-only model evaluated under mixed spatiotemporal conditions, indicating that period-specific modeling can reduce the influence of temporal variability on hyperspectral salinity inversion. Moreover, the absence of a detectable performance degradation when proxy labels were used suggests that fusion-derived proxy labels have potential as an efficient source of supervision for regional soil salinity inversion. Nevertheless, their equivalence to conventional gravimetric labels should not be inferred solely from the non-significant Wilcoxon test and would require further validation using dedicated equivalence testing or additional independent observations.

Table Ⅲ Performance comparison of hyperspectral regional inversion models across different periods and label sources. The table presents the mean ± standard deviation of R^2 and RMSE for each period, along with the mean difference between proxy and gravimetric labels and the corresponding Wilcoxon test P-values.

Period	Metric	Gravimetric Label	Proxy Label	Mean Difference	P-value
T1	R^2	0.847±0.109	0.891±0.108	+0.044	1
T1	RMSE(g/kg)	11.244±1.992	6.770±1.070	−4.474	0.0625
T2	R^2	0.875±0.078	0.873±0.081	−0.002	1
T2	RMSE(g/kg)	8.717±2.649	9.532±3.355	+0.815	1
T3	R^2	0.878±0.047	0.828±0.092	−0.050	1
T3	RMSE(g/kg)	11.368±3.371	14.210±3.899	+2.842	0.8125
T4	R^2	0.962±0.013	0.936±0.020	−0.026	1
T4	RMSE(g/kg)	6.688±1.436	8.779±0.981	+2.091	0.125
T5	R^2	0.788±0.155	0.802±0.088	+0.014	1
T5	RMSE(g/kg)	10.330±1.993	8.325±0.520	−2.005	0.1875
T6	R^2	0.787±0.163	0.711±0.185	−0.076	1
T6	RMSE(g/kg)	5.059±1.693	6.776±2.422	+1.717	0.0625

3.4 Regional-Scale Soil Salinity Mapping and Temporal Variation Analysis

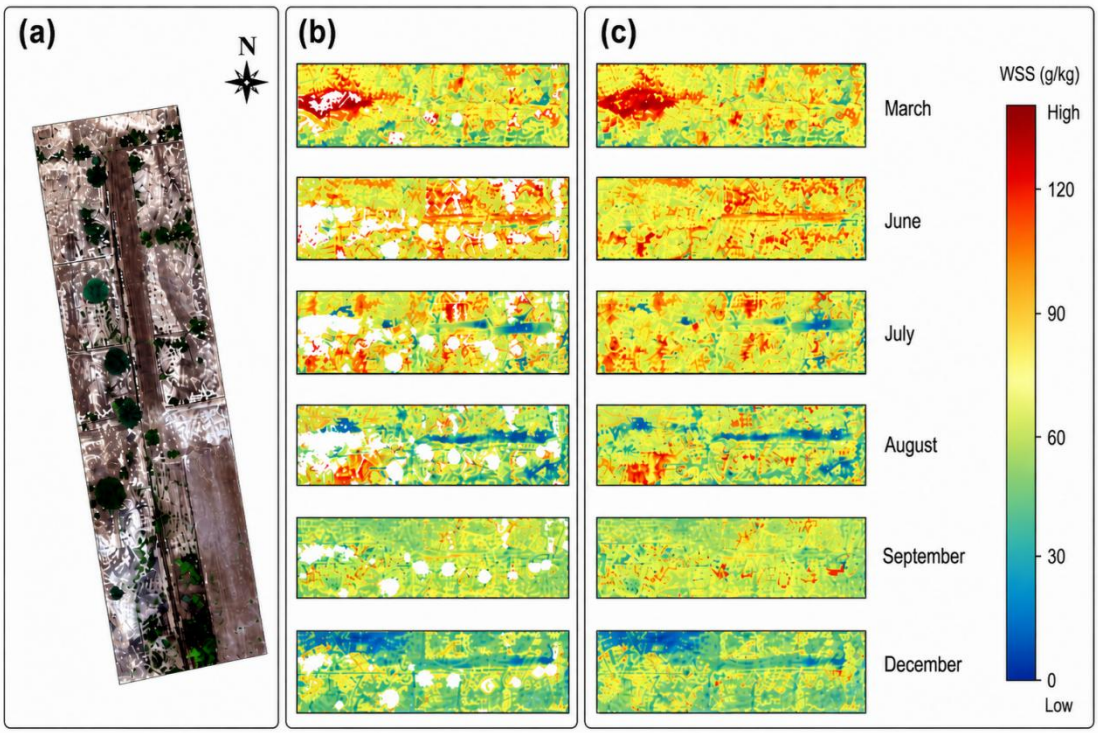


Fig. 7 Regional inversion and mapping results of soil water-soluble total salt content in the study area. (a) Original RGB image of the study area; (b) hyperspectral regional inversion results after SAVI masking; and (c) hyperspectral regional inversion results after spatial gap filling. Colors represent soil water-soluble total salt content (WSS, g/kg), with values increasing from blue to red. From top to bottom, the subpanels correspond to the regional inversion results for different periods from March to December.

To further evaluate the spatial continuity and reliability of regional inversion results, as well as to characterize the intra-annual temporal variations of surface soil water-soluble total salt content in the study area, spatial gap filling was applied to the masked regional inversion results. The spatial distribution patterns and seasonal evolution were then analyzed based on the visualized results for different periods. This section addresses two main questions: first, whether the regional salinity maps, after vegetation masking and spatial gap filling, can reliably and continuously represent the spatial patterns of soil salinity in the study area; second, whether surface soil salinity exhibits consistent seasonal variations and corresponding spatial differences across different periods. The results are presented in Fig. 7.

By comparing Fig. 7(a) and Fig. 7(b), it can be observed that applying the Soil-Adjusted Vegetation Index (SAVI) for spectral masking of hyperspectral images effectively identified and removed vegetated areas, while the bare-soil-dominated target regions were well preserved. This indicates that SAVI masking can effectively reduce the interference of vegetation cover on soil salinity inversion results, providing a cleaner and more reliable spectral basis for subsequent spatial inversion and visualization of water-soluble total salt content.

As shown in Fig. 7(c), spatial gap filling improved the continuity of the regional salinity maps by assigning estimated values to pixels excluded during vegetation masking. The imputed values generally followed the spatial variation of neighboring valid soil pixels, thereby reducing discontinuities in the mapped salinity distribution. It should be emphasized, however, that pixels removed by the SAVI-based vegetation mask were not directly predicted from hyperspectral observations. Instead, their WSTS values were spatially estimated from surrounding valid soil pixels using the gap-filling procedure. Therefore, the values in these masked areas should be interpreted as spatially imputed estimates rather than direct HSI-based inversion results. Accordingly, the gap-filled maps are primarily intended to facilitate visualization of the continuous regional salinity pattern, while the directly inverted pixels provide the primary spectral evidence for soil salinity estimation

In terms of spatial distribution, surface soil water-soluble total salt content in the study area exhibited distinct temporal variation across different periods.During the observation year, surface soil WSTS exhibited an intra-annual pattern characterized by relatively higher values during spring and summer and lower values during autumn and winter. For instance, in the Baidunzi Basin of the Jingdian Irrigation District, the mean annual precipitation is approximately 185.7 mm, primarily concentrated between May and September, while the mean annual evaporation can reach 2516 mm(Wang et al., 2021). Under this “low-precipitation–high-evaporation” climate, surface soil salinity tends to accumulate. During spring and summer, increasing temperatures and enhanced evaporation drive upward capillary water movement, transporting dissolved salts to the surface and leading to an enrichment of surface soil water-soluble total salt content(Lazarovitch et al., 2023). In contrast, during autumn and winter, lower temperatures and reduced evaporation, combined with precipitation events, promote downward leaching of salts, thereby decreasing surface salinity levels.

Regarding spatial heterogeneity, in summer and autumn, the combined effects of precipitation, irrigation, and local runoff result in relatively active water–salt redistribution, facilitating the formation of patchy salinity patterns across the region. In winter, however, both precipitation and evaporation are weak, limiting water–salt movement and reducing spatial differences in surface salinity, leading to more uniform distribution. This observation aligns with long-term monitoring studies, which indicate that seasonal accumulation and leaching of soil salinity in arid irrigation districts are jointly controlled by potential evapotranspiration, water inputs, and groundwater conditions, with spatial heterogeneity adjusting according to the intensity of water–salt redistribution(G. Liu et al., 2022)

In summary, the regional inversion results for soil water-soluble total salt content demonstrate good spatial continuity and reflect the seasonal pattern of higher salinity in spring and summer and lower salinity in autumn and winter. These findings indicate that the constructed regional inversion and mapping approach effectively captures the spatiotemporal distribution of soil salinity in the study area, providing intuitive and reliable spatial information to support subsequent monitoring and dynamic management of saline–alkaline lands.

4. **Conclusions**

This study developed a soil salinity monitoring framework integrating Laser-Induced Breakdown Spectroscopy (LIBS) and unmanned aerial vehicle hyperspectral imaging (UAV-HSI), enabling synergistic analysis from point-scale salinity prediction to regional inversion and temporal mapping.

The results indicate that LIBS features effectively capture salinity-related elemental information, while HSI sensitive bands and spectral indices reflect spectral responses induced by surface salt accumulation. Multi-source feature fusion significantly improved model performance, demonstrating strong complementarity between the two techniques. At the point scale, LIBS mitigates the interference caused by spatiotemporal heterogeneity and, in combination with HSI, achieves optimal predictive performance under complex spatiotemporal conditions, outperforming single-source models.

Moreover, regional inversion models constructed within the same period exhibited good stability and spatial extrapolation capability. The inversion accuracy obtained using fusion-derived labels was comparable to that achieved with conventional gravimetric labels, indicating that fusion labels can serve as an effective alternative to traditional chemical measurements. Regional mapping results effectively revealed the spatial distribution patterns of soil salinity and the seasonal variation, with higher salinity in spring – summer and lower salinity in autumn – winter.

Overall, the integration of LIBS and UAV-HSI provides an effective approach for high-precision, regional, and dynamic monitoring of soil salinity in complex field environments, offering reliable technical support for the precision management of saline – alkaline farmland.

CRediT authorship contribution statement

Guanghui dong: Conceptualization; Data curation; Formal analysis; Investigation; Methodology;Software; Validation; Visualization; Writing – original draft; Writing – review & editing. Kadambot H. M. Siddique: Writing – review & editing. Weiwei Han: Investigation. Guoding Zhang: Funding acquisition. Andong Wang: Data curation; Investigation. Shaoping Du: Funding acquisition. Juan Chen: Software; Writing – review & editing. Chaonan Tang: Supervision. Maogen Su: Conceptualization; Funding acquisition; Resources; Writing – review & editing

Declaration of competing interest

The authors declare that they have no known competing financial interests or personal relationships that could have appeared to influence the work reported in this paper.

Acknowledgements

This work was supported by the Science and Technology Department of Gansu Province (Grant No. 22ZD6FA021-5), the National Key R&D Program of China (Grant No. 2023YFD2301100), the National Natural Science Foundation of China (Grant No. 12464036), Lanzhou Youth Science and Technology Talents Project (Grant No. 2024-QN-102), and the Gansu Provincial Department of Education (Grant No. 2025CXZX-271).

References

Bannari, A., El-Battay, A., Bannari, R., Rhinane, H., 2018. Sentinel-MSI VNIR and SWIR Bands Sensitivity Analysis for Soil Salinity Discrimination in an Arid Landscape. Remote Sensing 10, 855. https://doi.org/10.3390/rs10060855

Bañón, S., Álvarez, S., Bañón, D., Ortuño, M.F., Sánchez-Blanco, M.J., 2021. Assessment of soil salinity indexes using electrical conductivity sensors. Scientia Horticulturae 285, 110171. https://doi.org/10.1016/j.scienta.2021.110171

Borsoi, R.A., Imbiriba, T., Bermudez, J.C.M., 2020. A Data Dependent Multiscale Model for Hyperspectral Unmixing With Spectral Variability. IEEE Transactions on Image Processing 29, 3638–3651. https://doi.org/10.1109/TIP.2020.2963959

Chen, Q., Vaudour, E., Richer-de-Forges, A.C., Arrouays, D., 2025. Spectral indices in remote sensing of soil: definition, popularity, and issues. A critical overview. Remote Sensing of Environment 329, 114918. https://doi.org/10.1016/j.rse.2025.114918

Chicco, D., Warrens, M.J., Jurman, G., 2021. The coefficient of determination R-squared is more informative than SMAPE, MAE, MAPE, MSE and RMSE in regression analysis evaluation. PeerJ Computer Science 7, e623. https://doi.org/10.7717/peerj-cs.623

Corwin, D.L., Lesch, S.M., 2005. Apparent soil electrical conductivity measurements in agriculture. Computers and Electronics in Agriculture 46, 11–43. https://doi.org/10.1016/j.compag.2004.10.005

Corwin, D.L., Scudiero, E., 2019. Review of soil salinity assessment for agriculture across multiple scales using proximal and/or remote sensors. Advances in Agronomy 158, 1–130. https://doi.org/10.1016/bs.agron.2019.07.001

Das, A., Bhattacharya, B.K., Setia, R., Jayasree, G., Sankar Das, B., 2023. A novel method for detecting soil salinity using AVIRIS-NG imaging spectroscopy and ensemble machine learning. ISPRS Journal of Photogrammetry and Remote Sensing 200, 191–212. https://doi.org/10.1016/j.isprsjprs.2023.04.018

Dehaan, R.L., Taylor, G.R., 2002. Field-derived spectra of salinized soils and vegetation as indicators of irrigation-induced soil salinization. Remote Sensing of Environment 80, 406–417. https://doi.org/https://doi.org/10.1016/S0034-4257(01)00321-2

Douaoui, A.E.K., Nicolas, H., Walter, C., 2006. Detecting salinity hazards within a semiarid context by means of combining soil and remote-sensing data. Geoderma 134, 217–230. https://doi.org/10.1016/j.geoderma.2005.10.009

753 Fernández-Buces, N., Siebe, C., Cram, S., Palacio, J.L., 2006. Mapping soil salinity using a
754 combined spectral response index for bare soil and vegetation: A case study in the
755 former lake Texcoco, Mexico. Journal of Arid Environments 65, 644-667.
756 https://doi.org/10.1016/j.jaridenv.2005.08.005
757 Goueguel, C.L., Soumare, A., Nault, C., Nault, J., 2019. Direct determination of soil texture
758 using laser-induced breakdown spectroscopy and multivariate linear regressions.
759 Journal of Analytical Atomic Spectrometry 34, 1588-1596.
760 https://doi.org/10.1039/C9JA00090A
761 Hao, Z., Berman, M., Guo, Y., Stone, G., Johnstone, I., 2016. Semi-realistic Simulations of
762 Natural Hyperspectral Scenes. IEEE Journal of Selected Topics in Applied Earth
763 Observations and Remote Sensing 9, 4407-4419.
764 https://doi.org/10.1109/JSTARS.2016.2580178
765 Hassani, A., Azapagic, A., Shokri, N., 2021. Global predictions of primary soil salinization
766 under changing climate in the 21st century. Nature Communications 12, ）.
767 https://doi.org/10.1038/s41467-021-26907-3
768 He, Y., Li, H., Zhang, M., Liu, S., Zhu, C., Xin, B., Wang, J., Wu, Q., 2025. Hyperspectral and
769 Multispectral Remote Sensing Image Fusion Based on a Retractable Spatial-Spectral
770 Transformer Network. Remote Sensing 17, 1973. https://doi.org/10.3390/rs17121973
771 He, Y., Zhang, Z., Xiang, R., Ding, B., Du, R., Yin, H., Chen, Y., Ba, Y., 2023. Monitoring salinity
772 in bare soil based on Sentinel-1/2 image fusion and machine learning. Infrared
773 Physics & Technology 131, 104656. https://doi.org/10.1016/j.infrared.2023.104656
774 Howari, F.M., Goodell, P.C., Miyamoto, S., 2002. Spectral Properties of Salt Crusts Formed on
775 Saline Soils. Journal of Environmental Quality 31, 1453-1461. https://doi.org/DOI:
776 10.2134/jeq2002.1453
777 Ivushkin, K., Bartholomeus, H., Bregt, A.K., Pulatov, A., Kempen, B., de Sousa, L., 2019. Global
778 mapping of soil salinity change. Remote Sensing of Environment 231, 111260.
779 https://doi.org/10.1016/j.rse.2019.111260
780 Jiao, T., Wu, J., Zhao, S., Li, Y., Zhao, G., Lei, Z., 2018. Distribution and utilization of nitrogen on
781 moderately and heavily grazed temperate desert steppe using the 15N tracing
782 technique. Applied Soil Ecology 124, 69-74.
783 https://doi.org/10.1016/j.apsoil.2017.10.030
784 Kahaer, Y., Tashpolat, N., 2019. Estimating Salt Concentrations Based on Optimized Spectral
785 Indices in Soils with Regional Heterogeneity. Journal of Spectroscopy 2019, 1-15.
786 https://doi.org/10.1155/2019/2402749
787 Khan, N.M., Rastoskuev, V.V., Sato, Y., Shiozawa, S., 2005. Assessment of hydrosaline land
788 degradation by using a simple approach of remote sensing indicators. Agricultural
789 Water Management 77, 96-109. https://doi.org/10.1016/j.agwat.2004.09.038
790 Lazarovitch, N., Kisekka, I., Oker, T.E., Brunetti, G., ohling, T.W., Xianyue, L., Yong, L., Skaggs,
791 ToddH., Furman, A., Sasidharan, S., 2023. Modeling of irrigation and related
792 processes with HYDRUS, in: Advances in Agronomy. pp. 79-181.
793 https://doi.org/10.1016/bs.agron.2023.05.002
794 Li, X., Xu, Z., Zhang, P., Guo, Z., Wu, Y., Gao, L., Wang, Q., 2025. Accurate quantitative
795 detection of sodium (Na) content in sorghum roots based on multi-source data fusion
796 of LIBS and HSI. Food Chemistry 492, 145446.

https://doi.org/10.1016/j.foodchem.2025.145446
Lin, N., Ma, X., Sui, Y., Zhu, R., Liu, H., Wu, M., Jiang, R., 2026. Soil salinity estimation based on satellite hyperspectral and synthetic aperture radar remote sensing image fusion. Agricultural Water Management 323, 110076. https://doi.org/10.1016/j.agwat.2025.110076
Lin, P., Song, C., Yang, C., Zhang, M., Ma, S., Wen, J., Dong, D., Han, Y., 2024. Rapid and accurate detection of total nitrogen in the different types for soil using laser-induced breakdown spectroscopy combined with transfer learning. Computers and Electronics in Agriculture 226, 109396. https://doi.org/10.1016/j.compag.2024.109396
Liu, G., Wang, C., Wang, X., Huo, Z., Liu, J., 2022. Growing season water and salt migration between abandoned lands and adjacent croplands in arid and semi-arid irrigation areas in shallow water table environments. Agricultural Water Management 274, 107968. https://doi.org/10.1016/j.agwat.2022.107968
Liu, Y., Zhao, S., Gao, X., Fu, S., Dou, Y., Qi, C., Lin, J., 2022. Combined laser-induced breakdown spectroscopy and hyperspectral imaging with machine learning for the classification and identification of rice geographical origin. RSC Advances 12, 34520-34530. https://doi.org/10.1039/D2RA06892C
Lu, B., Dao, P., Liu, J., He, Y., Shang, J., 2020. Recent Advances of Hyperspectral Imaging Technology and Applications in Agriculture. Remote Sensing 12, 2659. https://doi.org/10.3390/rs12162659
Metternicht, G.I., Zinck, J.A., 2003. Remote sensing of soil salinity: potentials and constraints. Remote Sensing of Environment 85, 1-20. https://doi.org/https://doi.org/10.1016/S0034-4257(02)00188-8
Pessoa, L.G.M., Dos Santos Freire, M.B.G., Wilcox, B.P., Rossi, C.G., Souza, A.M.D.O., Galví ncio, J.D., 2015. Spectral Reflectance Characteristics of Laboratory-Grown Salt Crusts on Silty Clay and Sandy Soils. Communications in Soil Science and Plant Analysis 46, 1895-1904. https://doi.org/10.1080/00103624.2015.1059849
Ren, J., Zhao, Y., Yu, K., 2022. LIBS in agriculture: A review focusing on revealing nutritional and toxic elements in soil, water, and crops. Computers and Electronics in Agriculture 197, 106986. https://doi.org/10.1016/j.compag.2022.106986
Saleh, J., Najafi, N., Oustan, S., Aliasgharzad, N., Ghassemi-Golezani, K., 2013. Changes in Extractable Si, Fe, and Mn as Affected by Silicon, Salinity, and Waterlogging in a Sandy Loam Soil. Communications in Soil Science and Plant Analysis 44, 1588-1598. https://doi.org/10.1080/00103624.2013.768261
Schober, P., Boer, C., Schwarte, L.A., 2018. Correlation Coefficients: Appropriate Use and Interpretation. Anesthesia & Analgesia 126, 1763-1768. https://doi.org/10.1213/ANE.0000000000002864
Shoshany, M., Goldshleger, N., Chudnovsky, A., 2013. Monitoring of agricultural soil degradation by remote-sensing methods: a review. International Journal of Remote Sensing 34, 6152-6181. https://doi.org/10.1080/01431161.2013.793872
Si-Cun, Y., Huan-Cheng, P., Cheng-Bao, W., Yu-Yi, L., Lin, H., Wan-Li, J., 2014. Characterization of Soil Salinization Based on Canonical Correspondence Analysis Method in Gansu Yellow River Irrigation District of Northwest China. SCIENTIA

AGRICULTURA SINICA 47, 100-110. https://doi.org/10.3864/J.ISSN.0578-1752.2014.01.011

Song, Y., Gao, M., Wang, J., 2024. Inversion of salinization in multilayer soils and prediction of water demand for salt regulation in coastal region. Agricultural Water Management 301, 108970. https://doi.org/10.1016/j.agwat.2024.108970

Sun, J., Xu, F., Cervone, G., Gervais, M., Wauthier, C., Salvador, M., 2021. Automatic atmospheric correction for shortwave hyperspectral remote sensing data using a time-dependent deep neural network. ISPRS Journal of Photogrammetry and Remote Sensing 174, 117-131. https://doi.org/DOI: 10.1016/j.isprsjprs.2021.02.007

Tang, H., Xiao, C., Shang, K., Wu, T., Li, Q., 2023. Radiometric Calibration of GF5-02 Advanced Hyperspectral Imager Based on RadCalNet Baotou Site. Remote Sensing 15, 2233. https://doi.org/10.3390/rs15092233

Villas - Boas, P.R., Franco, M.A., Martin - Neto, L., Gollany, H.T., Milori, D.M.B.P., 2020. Applications of laser - induced breakdown spectroscopy for soil characterization, part II: Review of elemental analysis and soil classification. European Journal of Soil Science 71, 805-818. https://doi.org/10.1111/ejss.12889

Wang, L., Zhang, B., Shen, Q., Yao, Y., Zhang, S., Wei, H., Yao, R., Zhang, Y., 2021. Estimation of Soil Salt and Ion Contents Based on Hyperspectral Remote Sensing Data: A Case Study of Baidunzi Basin, China. Water 13, 559. https://doi.org/10.3390/w13040559

Wang, T., Dong, J., Lyu, B., Gao, X., Wang, N., Shi, Z., 2025. High-resolution global soil salinity and sodicity mapping (1980-2024): Box-Cox-based sample optimization, multi-source remote sensing features, and uncertainty quantification. Remote Sensing of Environment 330, 114991. https://doi.org/10.1016/j.rse.2025.114991

Yu, J., Li, Y., Ge, D., Chen, Y., Wu, Q., Ma, Y., 2024. Efficient Geometric Correction Workflow for Airborne Hyperspectral Images through DEM-Driven Correction Techniques. The International Archives of the Photogrammetry, Remote Sensing and Spatial Information Sciences XLVIII-1-2024, 831-836. https://doi.org/10.5194/isprs-archives-XLVIII-1-2024-831-2024

Zhan, D., Liu, Y., Yang, W., Lu, M., Song, Y., 2025. Spatial variability of soil salinity in coastal saline-alkali farmlands: A novel approach integrating a stacked model with the reconstructed in-situ hyperspectral feature. Computers and Electronics in Agriculture 235, 110376. https://doi.org/10.1016/j.compag.2025.110376

Zhang, D., Tiyip, T., Ding, J., Zhang, F., Nurmemet, I., Kelimu, A., Wang, J., 2016. Quantitative Estimating Salt Content of Saline Soil Using Laboratory Hyperspectral Data Treated by Fractional Derivative. Journal of Spectroscopy 2016, 1-11. https://doi.org/10.1155/2016/1081674

ZHAO, M., YAN, C., FENG, Y., XUE, J., TANG, H., ZHANG, T., LI, H., 2020. A novel strategy for quantitative analysis of soil pH via laser-induced breakdown spectroscopy coupled with random forest. Plasma Science and Technology 22, 074003. https://doi.org/10.1088/2058-6272/ab6ac2

Zhao, S., Song, W., Hou, Z., Wang, Z., 2021. Classification of ginseng according to plant species, geographical origin, and age using laser-induced breakdown spectroscopy and hyperspectral imaging. Journal of Analytical Atomic Spectrometry 36, 1704-1711. https://doi.org/10.1039/D1JA00136A

Zhao, S., Zhao, Y., Hou, Z., Wang, Z., 2023. Rapid and high-resolution visualization elements analysis of material surface based on laser-induced breakdown spectroscopy and hyperspectral imaging. Applied Surface Science 629, 157415. https://doi.org/10.1016/j.apsusc.2023.157415